applied sciences

MDPI

Article

Synthesis and Characterization of $ZnBi_2O_4$ Nanoparticles: Photocatalytic Performance for Antibiotic Removal under Different Light Sources

Oussama Baaloudj [1], Achraf Amir Assadi [2], Mohamed Azizi [3,4], Hamza Kenfoud [1], Mohamed Trari [1], Abdeltif Amrane [5,*], Aymen Amine Assadi [5] and Noureddine Nasrallah [1]

1 Laboratory of Reaction Engineering, Faculty of Mechanical Engineering and Process Engineering, USTHB, BP 32, Algiers 16111, Algeria; obaaloudj@gmail.com (O.B.); hamza.kenfoud.93@gmail.com (H.K.); mtrari@usthb.dz (M.T.); nas_nour@yahoo.fr (N.N.)
2 Higher Institute of Applied Sciences and Technology of Gabes (ISSAT), University of Gabes, Sfax 3018, Tunisia; achraf.assadi@gmail.com
3 Water Research and Technology Center, CERTE, Laboratory of Nature Water Treatment (LabTEN), BP 273, Soliman 8020, Tunisia; Aazizi.azzizmed@gmail.com
4 Faculty of Science and Arts-Qilwah, Albaha University, Qilwah 65941, Saudi Arabia
5 CNRS, Université Rennes, Ecole Nationale Supérieure de Chimie de Rennes, ISCR-UMR 6226, F-35000 Rennes, France; aymen.assadi@ensc-rennes.fr
* Correspondence: abdeltif.amrane@univ-rennes1.fr

Citation: Baaloudj, O.; Assadi, A.A.; Azizi, M.; Kenfoud, H.; Trari, M.; Amrane, A.; Assadi, A.A.; Nasrallah, N. Synthesis and Characterization of $ZnBi_2O_4$ Nanoparticles: Photocatalytic Performance for Antibiotic Removal under Different Light Sources. *Appl. Sci.* **2021**, *11*, 3975. https://doi.org/10.3390/app11093975

Academic Editors: Simone Morais and Carmen Zaharia

Received: 26 March 2021
Accepted: 26 April 2021
Published: 27 April 2021

Abstract: This work aims to synthesize a photocatalyst with high photocatalytic performances and explore the possibility of using it for antibiotic removal from wastewater. For that, the spinel $ZnBi_2O_4$ (ZBO) was produced with the co-precipitation method and its optical, dielectric, and electrochemical characteristics were studied. The phase has been determined and characterized by X-ray diffraction (XRD) and Fourier transform infrared spectroscopy (FT-IR). For the ZBO morphology, a Scanning Electron Microscopy (SEM) has been used. Then, the optical and dielectric properties of ZBO have been evaluated by calculating refractive index n (λ), extinction coefficient (k), dissipation factor (tan δ), relaxation time (τ), and optical conductivity (σopt) using the spectral distribution of T(λ) and R(λ). An optical gap band of 2.8 eV was determined and confirmed. The electrochemical performance of ZBO was investigated and an n-type semiconductor with a flat band potential of 0.54 V_SCE was found. The photocatalytic efficiency of ZBO was investigated in order to degrade the antibiotic Cefixime (CFX) under different light source irradiations to exploit the optical properties. A high CFX degradation of approximately 89% was obtained under solar light (98 mW cm^{-2}) only after 30 min, while 88% of CFX degradation efficiency has been reached after 2 h under UV irradiation (20 mW cm^{-2}); this is in line with the finding of the optical characterizations. According to the obtained data, solar light assisted nanoparticle ZBO can be used successfully in wastewater to remove pharmaceutical products.

Keywords: spinel $ZnBi_2O_4$; optical properties; dielectric constants; electrochemical proprieties; photocatalysis

1. Introduction

In the last few years, numerous synthetic drugs have contaminated the aqueous system [1]. Antibiotics are the major problem among these contaminants, as they are highly toxic and widely used for both pets and human medicines [2]. They increase environmental pollution due to their widespread use and toxic nature [3]. Moreover, the presence of these compounds in water supplies, even at low levels, strengthens bacterial resistance, consequently creating antibiotic resistance (ABR) [4]. ABR is the ability to live and to multiply in the presence of antibiotic concentrations, which have previously been thought to be successful against a given bacterium or another microorganism [5]. New research has

found that antibiotic resistance is responsible for 700,000 deaths per year worldwide [6]. They are now generally recognized as a significant threat to public health [7].

The conventional wastewater treatment techniques cannot effectively eliminate residues of antibiotics from wastewater [8–10]. Examples of these physical treatment approaches, such as filtration, adsorption, reverse osmosis, and membrane, cannot remove antibiotics totally from wastewater that remains the risk of the cumulative contaminants as an environmental concern. However, it has been emphasized that Advanced Oxidation Processes (AOPs) are a viable alternative to the rapid degradation of non-degradable compounds in water [11–14]. The heterogeneous photocatalytic technique has especially shown an efficient degradation of various drug forms and organic molecules [15–21]. It is based on the concept of catalyst activation utilizing energy given by a light source, such as LED, UV, and solar light [22]. Semiconductors are widely used as catalysts, because they are efficient and straightforward to synthesize. The preferred materials for the synthesis of the semiconductors are titanium (Ti), bismuth (Bi), zinc (Zn), and tin (Sn) [23–25], and as examples, ZnO and TiO_2 semiconductors, which are commonly used. Recently, Bismuth-based semiconductors have become a promising group of developed advanced photocatalytic materials due to their high chemical stability and their excellent transparency for light penetration [26,27]. Zinc bismuthate with the chemicals formula $ZnBi_2O_4$ (ZBO) is a topical semiconductor and promising photocatalyst that has attracted interest among several research groups [26,28–32]. That is due to its high stability and small optical band gap around 2.8 eV, making better use of sun-light.

In the comparison between ZBO, zinc oxide (ZnO) and bismuth oxide (Bi_2O_3), ZnO needs wavelengths below 400 nm for excitation due to its large bandgap, which gives it a low efficient harvester of sunlight, unlike ZBO which has a smaller one. This makes it more active in the sun-light and suitable for high photo-durability in various areas such as optoelectronics and photocatalysis [28,29]. On the other hand, Bi_2O_3 exhibits low photocatalytic activity due to the excited electrons from the conduction band (E_{CB} = 0.33 eV) that cannot produce active degradation radicals [33,34]. Another disadvantage of ZnO and Bi_2O_3 is that charge carrier recombination of photo-generated electron/hole pairs occurs in nanoseconds promoting photochemical corrosion [35]. In contrast, ZBO has an excellent charge carrier recombination rate, shielding it from photo-oxidation [36]. To our knowledge, this is the first application of ZBO for antibiotics removal. Moreover, there is a lack of studies dealing with the use of ZBO as a photocatalyst and only one study has dealt with the electrochemical characterization of ZBO (only Mott-Schottky characteristic [37]). Moreover, no studies have been carried out yet on the optical and dielectric properties of ZBO.

Cefixime (CFX) with the molecular formula $C_{16}H_{15}N_5O_7S_2$ was selected for this research as a standard example of antibiotics known as third cephalosporin antibiotics semi-synthetically extracted from the marine fungus [38,39]. The molecular composition listed above is shown in Figure S1 in the Supplementary Data.

We mentioned in this research the synthesis of the photocatalyst $ZnBi_2O_4$ developed through the co-precipitation process. The phase was identified using X-ray diffraction (XRD) and Fourier transform infrared spectroscopy (FT-IR). After that, we investigated ZBO's optical and dielectric properties, which are measured using diffuse reflectance R (λ). The electrochemical analysis was also conducted to classify the type of ZBO. Finally, the photocatalytic efficiency of the nano-powders ZBO was tested for the removal of Cefixime under different sources of light (UV, LED and solar light) in order to determine the ideal criteria for rapid degradation of CFX.

2. Materials and Methods

2.1. Chemicals

The products used in the following sections were bismuth nitrate pentahydrate [$Bi(NO_3)_3{\cdot}5H_2O$] (98.5% Chem-Lab), zinc nitrate hexahydrate [$N_2O_6Zn{\cdot}6H_2O$] (98% Biochem), cefixime trihydrate (Algerian pharmaceutical industry Pharmalliance), ammonia from Biochem, and ethanol, nitric acid, NaOH, and HCl from Sigma Aldrich.

2.2. Synthesis of $ZnBi_2O_4$ Nanoparticles

$ZnBi_2O_4$ (ZBO) nanoparticles were produced by chemical co-precipitation. The mixture was taken utilizing molar ratio amounts (ratio 1:2) of hexahydrate zinc nitrate [$N_2O_6Zn{\cdot}6H_2O$] and bismuth nitrate pentahydrate [$Bi(NO_3)_3{\cdot}5H_2O$] dissolved separately in ethanol with a magnetic stirring. In addition to the mixtures, excess 5% nitric acid was poured. The two solutions were combined and put on a hot plate at 50 °C for one hour after absolute solubility. Then, the NaOH 6 M solution was mixed well into the mixture to maintain the pH between 9 and 10. The creation of ZBO spinel was immediately confirmed by white precipitation. Consequently, the residue has been drained and washed with purified water several times, then dried in an autoclave at 120 °C for 24 h. The amorphous powder was shattered in an agate mortar to raise the amount of crystallization to a fine powder and then calcined 600 °C for 6 h in a standard furnace. Finally, the end product with a whitish-yellow color has been submitted to the identification step, optical, dielectric, and electrochemical characterizations.

2.3. Characterization

The X-ray diffraction (XRD) was performed with a Phillips PW 1730 in the 2θ range (5–80°). With an Alpha Bruker spectrometer, ATR-FTIR spectra were attained within the scope of 400–4000 cm^{-1}. The nanoparticles morphology was studied using electron scanning microscope SEM (FEI Quanta 650) attached by EDX analysis with a 20 kV scan rate. The sample's UV-visible diffuse reflectance spectrum (DRS) was analyzed by Cary 5000 UV-vis with dry pressed disk samples. In electrochemical analysis, the electrical contact on the back of the pellet was made from copper and silver paint. Then, the pellet was covered with epoxy resin in a glass tube. The research was conducted using three-electrode (the working electrode ZBO, Pt as counter electrode and Ag/AgCl (4 M KCl) as reference) in NaOH (0.1 M) solution. In the potential range (−1 to +1 V), the current-potential J(E) curves were obtained by the potentiostat PGZ 301 at a scan rate of 10 mV/s, in contrast, the capacity-potential (C^{-2}-E) characteristic was obtained at 10 kHz. In the range (10^{-1} to 10^5 Hz), electrochemical impedance spectroscopy (EIS) has been investigated.

2.4. Photocatalytic Degradation Study

In order to analyze the photocatalytic efficiency of $ZnBi_2O_4$, Cefixime was picked as a model pharmaceutical pollutant. The photocatalytic degradation of CFX was carried out after optimizing the parameters such as pH and dose of the catalyst by sets of experiments. The optimal photocatalytic reaction conditions were found to be pH 6 and 1 g/L catalyst dose. Then, the photocatalytic removal tests under different light sources were performed by mixing a quantity of ZBO (0.1 g) in a CFX mixture of about 100 mL with an initial concentration of 10 mg/L. In a reactor in dark conditions, the received suspension was stirred for 120 min to balance adsorption and desorption before irradiation. As light sources, UV (Ultraviolet light UVA 24 W (Philips PL/L), 270 nm, 20 mW/cm^2), LED (LEDs 50 W, 420 to 700 nm, 10.5 mW/cm^2) and solar light (coordinates 36°46′34″ Nord, 3°03′36″ est, time from 9 to 12 AM with intensity 98 mW/cm^{-2}) were applied separately to test the optical properties of ZBO. 3 mL samples were regularly removed from the blend and the precipitates were centrifuged for 10 min at a speed of 5000 rpm, then they were analyzed by UV-Visible spectrometry (OPTIZEN, UV-3220UV) with 1-cm matched quartz cells. The contaminant degradation was indicated by the band's loss relating to CFX at the highest absorption wavelength (λ = 288 nm), as illustrated in Figure S2 in the Supplementary Data.

The method of spectrophotometric determination of CFX was followed as mentioned in a previous paper [40]. The degradation was calculated with the following equation:

$$\text{Photodegradation } \% = \frac{(C_{Ad} - C(t))}{C_{Ad}} \times 100 \quad (1)$$

where C_{Ad} (mg/L) and $C(t)$ (mg/L) are the initial concentration after adsorption and the concentration at time t, respectively.

3. Results

3.1. Catalyst Characterization

3.1.1. Phase Identification and Characterization

The single phase of ZBO was proved to base on the X-ray diffraction (XRD) (Figure 1). Indeed, the phase of ZBO nano-powders was obtained at 600 °C almost a single. All peaks are narrow, indicating a good crystallization. The ZBO phase can be determined by diffraction peaks that are in strong agreement with previous research peaks [23,30]. Moreover, it conforms to the standard card (JCPDS No. 043-0449) of the tetragonal $ZnBi_2O_4$ [28]. The crystallite volume was estimated from the highest diffraction peaks using the following Debey–Scherer Equation (2). About 24.16 to 56.18 nm crystalline sizes have been found.

$$D = \frac{K\lambda}{\beta \cos(\theta)} \quad (2)$$

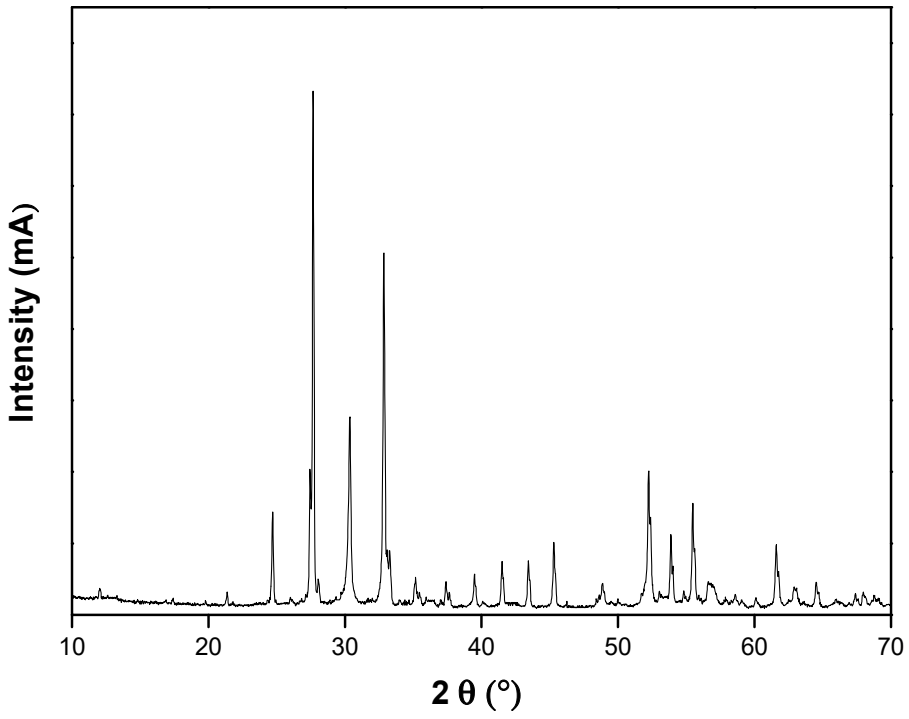

Figure 1. XRD diffractogram of $ZnBi_2O_4$ calcined at 600 °C.

D is the average crystallite size of the phase under examination in nanometers, K is the Scherrer constant (K = 0.9), λ is the wavelength of the X-ray beam used, β is the full width at half maximum (FWHM) in radians and θ is the Braggs angle.

The ZBO phase could be observed by Fourier transform infrared spectra, as shown in Figure 2. The spinel-shaped metal ions are identified in numerous separate sub-lattices recognized as A-site (tetrahedral) and B-site (octahedral). So, it can be identified in the FTIR analysis by Metal and the closest Oxygen neighbors of each element [41]. In our case,

the FTIR spectrum indicates the presence of three strong absorption bands in the region of 400–900 cm^{-1}, which might be associated with the band of metal-oxygen (M-O) [42–44]. The presence of these M-O bands means that the tetragonal structure is formed by zinc and bismuth oxides. The presence of peaks between 570 and 628 cm^{-1} confirmed the formation of spinel, which belonged to the vibration of the Bi–O bond [45,46]. The peaks that appear in 430 cm^{-1} and 524 cm^{-1} could be attributed to the tetrahedral (ZnO_4) in the catalyst [23,26].

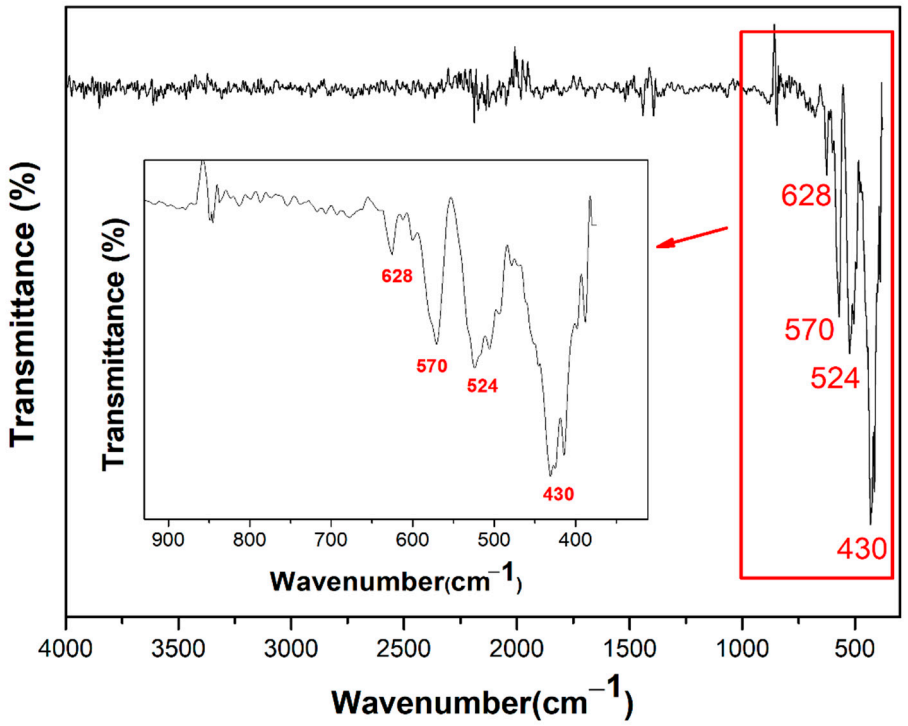

Figure 2. FTIR spectrum of $ZnBi_2O_4$.

3.1.2. Morphology Investigation

The morphology of nanoparticles ZBO was visualized on particles with well-defined morphology by Scanning Electron Micrograph (SEM) technique (Figure 3a). The study was carried out with an excellent enlargement (3 μm). It can be observed that the sample consisted of particles almost with the same morphology. It can also be seen particles of approximately 2 μm in size, corresponding to an agglomeration of nanoparticles; this can be demonstrated by the very tiny particles next to them. These particles had a slightly agglomerated morphology due to the ultra-finite nature of the sample. In addition, the Energy Dispersive X-ray technique (EDX) was done on the same SEM image location (Figure 3b). Only found peak the elements Zn, Bi and O were observed on the EDX spectrum and therefore no impurities. The inset table in Figure 3b identifies the atomic % of elements. As can be concluded, the Bi/Zn molar ratio is around 1.6 and the O/Zn molar ratio is about 3.9, indicating the composition of $ZnBi_2O_4$ nanoparticles.

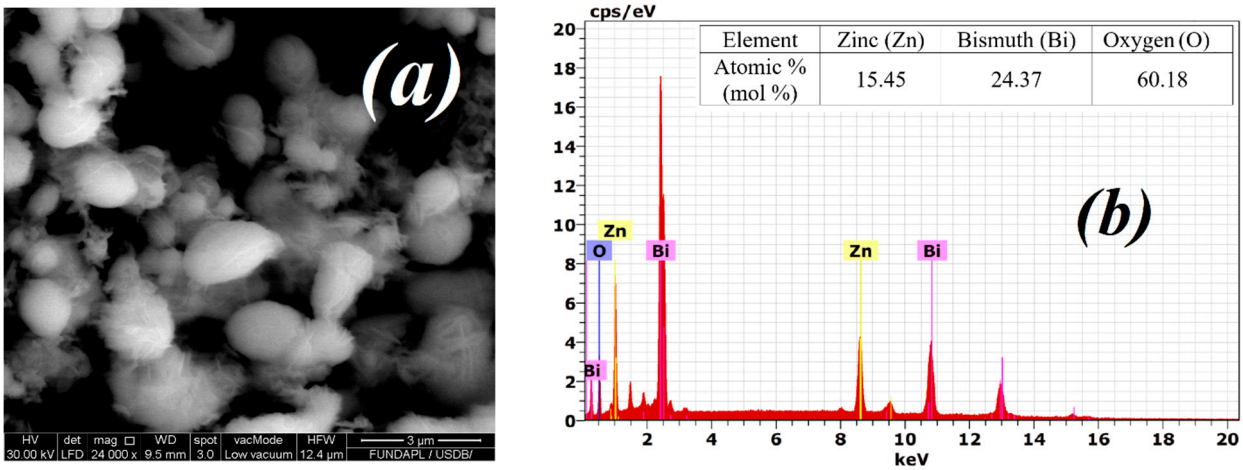

Figure 3. (**a**) SEM (**b**) Energy dispersive X-ray spectrum of $ZnBi_2O_4$.

3.1.3. Optical and Dielectric Proprieties

The optical characteristics of the $ZnBi_2O_4$ nanostructure were investigated using UV-vis diffuse reflectance spectroscopy (DRS). The spectral distribution of T(λ) and R(λ) were studied for ZBO in the wavelength range (200–900 nm) (Figure S3 in the Supplementary Data). The complex refractive index n̂ and the dielectric complex ε̂ characterize the optical properties of any solid material. They are presented in Equation (3) [47,48].

$$\hat{n} = n(\lambda) + iK(\lambda);\ \hat{\varepsilon} = \varepsilon r\ (\lambda) + i\varepsilon i\ (\lambda) \quad (3)$$

The imaginary and real parts of complex refractive n̂ are the refractive index n(λ) and absorption index (extinction) k(λ) and for the dielectric complex ε̂, are the normal dielectric constant εr(λ) and the absorption associated with radiation by free carrier εi (λ).

The extinction index k(λ) is calculated in terms of absorption α with the following equation [49]:

$$K(\lambda) = \frac{\alpha(\nu)\lambda}{4\pi};\ \alpha(\nu) = \alpha_0 e^{h\nu/E_u} \quad (4)$$

where λ, α(ν), α_0, h, E_u and n are wavelength, the absorption coefficient, a constant, the Plank's constant (6.63×10^{-34} J/s), the Urbach energy and the light frequency respectively.

And the refractive index n(λ) is calculated from the relation [50]:

$$n\ (\lambda) = \frac{(1 + R\ (\lambda) + \sqrt{4R\ (\lambda) - (1 - R\ (\lambda))^2\ K\ (\lambda)^2}}{1 - R\ (\lambda)} \quad (5)$$

The spectral dependences of both n (λ) and K (λ) as a function of wavelength are shown in Figure S4 in the supplementary data. The refractive index n (λ) decreases at the lower wavelengths and increases in the visible spectrum. This favors the optical properties in the UV region. For the extinction coefficient K (λ), the values are very small at the visible spectrum but increase at the lower wavelengths, which indicates that ZBO has a low dielectric loss in the UV region. The extinction coefficient attains a peak at a wavelength λ = 367 nm that is assigned to the fundamental energy gap.

For the dielectric real and imaginary parts, the normal dielectric constant εr(λ) and the absorption associated of radiation by free carrier εi (λ) are calculated from the refractive index n(λ) and absorption index K (λ) using the following equation [51]:

$$\varepsilon r\ (\lambda) = n(\lambda)^2 + K\ (\lambda)^2;\ \varepsilon i\ (\lambda) = 2\ n(\lambda)\ K\ (\lambda) \quad (6)$$

The variations of the dielectric constants εr and εi as functions of the energy (hν) are shown in Figure 4. The optical bandgap Eg value can be determined from this figure by extrapolating a straight line from the cross-point between the curves of the real and imaginary parts of the dielectric constant to the *x*-axis [51], which is equal to about 2.79 eV.

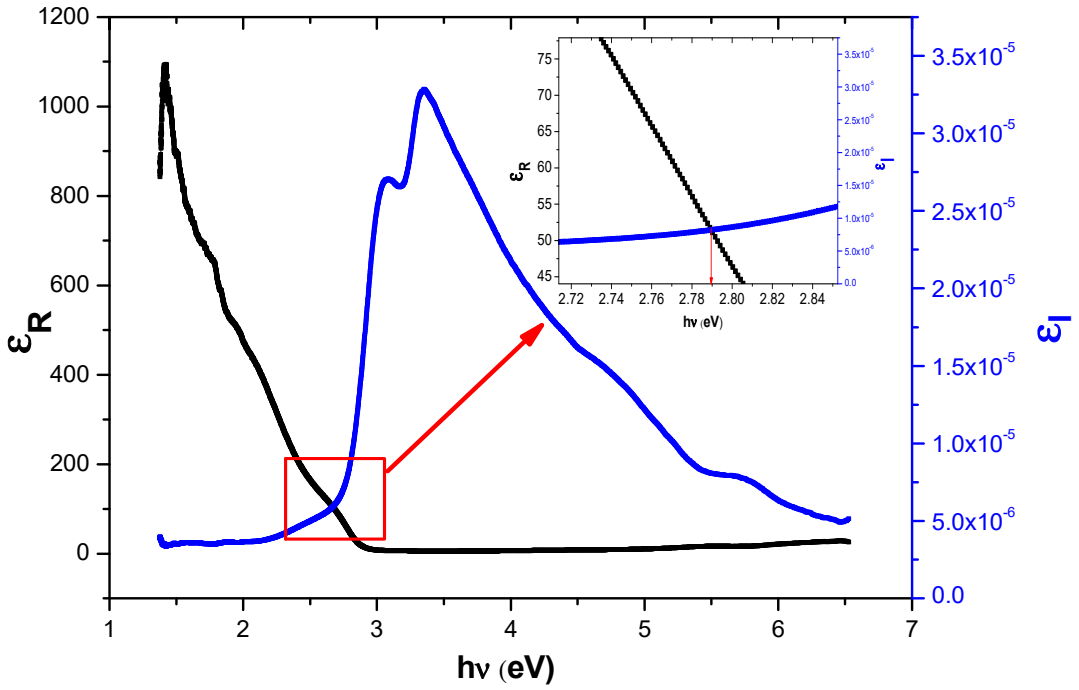

Figure 4. Dependence of the real and imaginary parts of the dielectric constant as a function of the energy.

The Surface and Volume energy loss functions (SELF and VELF) were calculated using the dielectric constants as the relations [52]:

$$\text{SELF} = \frac{\varepsilon i\ (\lambda)}{\left((\varepsilon r\ (\lambda)+1)^2+\varepsilon i\ (\lambda)^2\right)};\ \text{VELF} = \frac{\varepsilon i\ (\lambda)}{\left(\varepsilon r\ (\lambda)^2-\varepsilon i\ (\lambda)^2\right)} \tag{7}$$

The variations of the volume and the surface energy loss functions as functions of the energy (hν) are shown in Figure S5 in the Supplementary Data. The figure shows that both SELF and VELF are very small, especially at lower photon energies, almost equal to zero; this indicates that ZBO has a low dielectric loss.

The dissipation factor tan δ can measure the loss rate of electrical and mechanical power mode in all-dielectric materials, usually in the form of heat [51]. for that, the dissipation factor tan δ can characterize the energy lost as heat in the spinel oxides, which is calculated from the relation [53]:

$$\tan\ \delta = \frac{\varepsilon i\ (\lambda)}{\varepsilon r\ (\lambda)} \tag{8}$$

Figure 5a shows the change of tan δ as an energy function (hν). A significant increase in the range (2.4–2.9 eV) is shown in the dependency, clearly indicating that the activation level is located within this region. The band-gap energy Eg of ZBO was determined 2.78 eV, which is in agreement with the dielectric index values; this indicated that ZBO has a significant optical characteristic in the UV region because its band-gap is smaller than ZnO, which is widely recognized by its efficacy in the UV region [54].

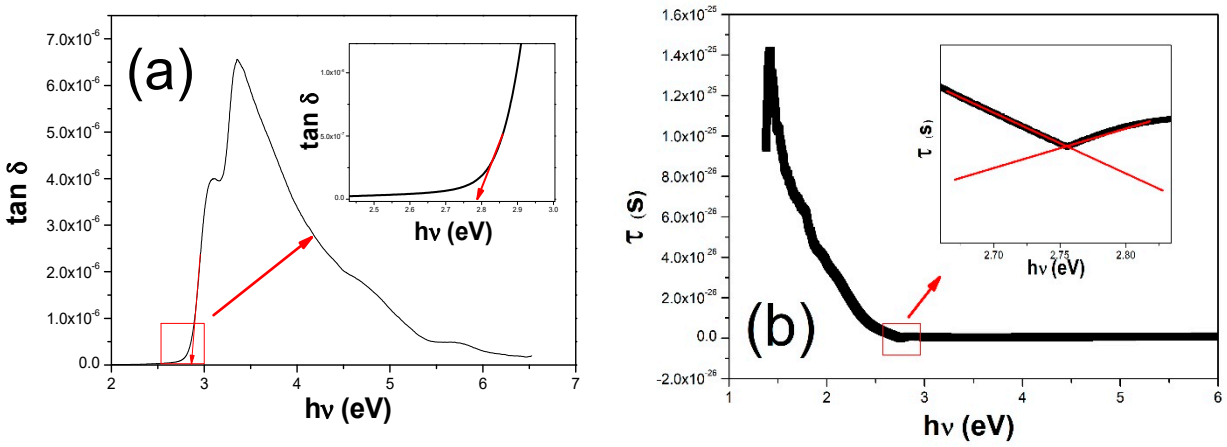

Figure 5. (**a**) the dissipation factor tan δ (**b**) the dielectric relaxation time τ as a function of the energy (hν).

The dielectric relaxation time τ allows to confirm the value of the optical bandgap Eg and also determine the limit of the recombination of the charge carrier, the relaxation time τ is calculated from the relation [55]:

$$|\tau| = \frac{\varepsilon_\infty - \varepsilon_r}{\omega \varepsilon_i} \quad (9)$$

ε_∞ is calculated using Equation (10) [51] and by drawing ε_r as a function of λ^2, as showing in Figure S6 in the Supplementary Data:

$$\varepsilon_r = \varepsilon_\infty - B\,\lambda^2;\ B = \frac{e^2 N}{4\pi^2 c^2 \varepsilon_0 m} \quad (10)$$

Figure 5b illustrated the dielectric relaxation time τ as a function of the energy (hν). The cross-point in the curve of dielectric relaxation time at hν = 2.76 eV may be attributed to the band-to-band absorption because this maximum occurs at hν = Eg which corresponds to the energy gap for ZBO. This is in agreement with the dielectric index and the dissipation factor gap values.

The optical bandgap value Eg can also be estimated and confirmed using the optical σopt as well as electrical σe conductivities of ZBO, which are calculated using the absorption coefficient α from the relations (11) [48]:

$$\sigma opt = \frac{\alpha n C}{4\pi}\ \sigma e = \frac{2\lambda \sigma opt}{\alpha} \quad (11)$$

where C is light velocity and α the absorption coefficient. Figure S7 in the Supplementary Data shows the variation of the optical σopt and electrical σe conductivities as a function of energy (hν). The cross-point between the curves in this figure confirmed once again the optical band gap Eg (~2.72 eV). This indicated that ZBO has good optical properties in the UV region, where the photons' conduction is the dominant mechanism.

3.1.4. Electrochemical Proprieties

As a preamble to the conversion of photo-energy, photocatalysis requires deep electrochemical characterization. It allows us, in particular, to better understand the semiconducting properties. ZBO Cyclic Voltammetry is intended to describe the stability of the semiconductor and determine the redox couple's specific potential. Figure 6 shows the density potential traced in the dark, the decrease current below (~−0.4 V), indicating a water reduction into hydrogen while the current rises over (~0.67 V) is due to oxygen evolution (O_2 + 2 H_2O + 2 e^- → H_2O_2). The significant difference between the peaks anodic and cathodic indicates a slow charge transfer which corresponds to a sluggish elec-

trochemical system and can be related to the irreversible electrochemical mechanism [56]. The semi-logarithmic characteristic (Tafel) in Figure S8 in the Supplementary Data gives a current exchange density of 3.14×10^{-7} mA cm^{-2} and a potential of -0.7 V, confirming good electrochemical stability in the basic medium.

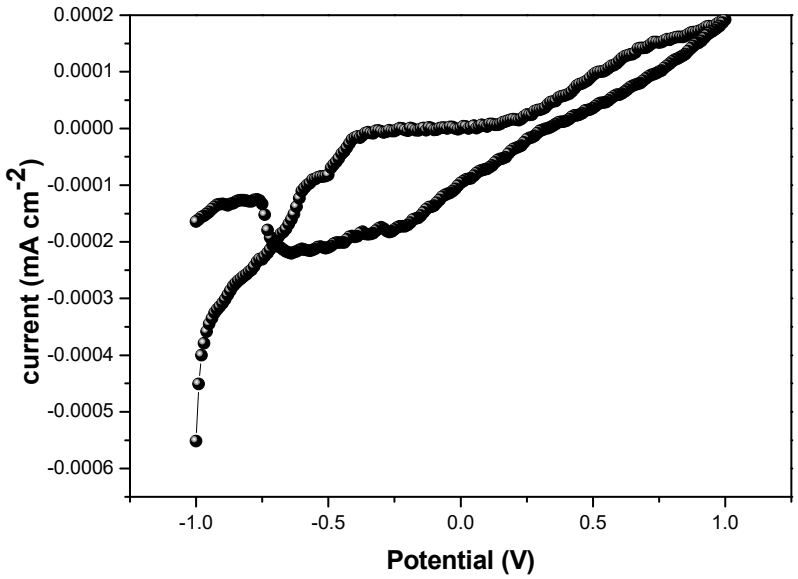

Figure 6. The cyclic J (E) voltammetry of $ZnBi_2O_4$ plotted in NaOH (0.1 M) with a scan rate of 10 mV s^{-1}.

Photo-electrochemistry offers knowledge about the properties of the semiconductor. The location of electronic bands has great importance for the prediction of interfacial reactions in photocatalysis, and it is located using the flat band potential. The flat band potential is determined from the capacitance-potential plot using the Mott–Schottky relation [57]:

$$C^{-2} = \frac{2}{e\varepsilon\varepsilon_0 A^2 N_D}\left(E - E_{fb} - \frac{kT}{e}\right) \quad (12)$$

where k is the Boltzmann constant, T the absolute temperature, kT the thermal energy (~26 meV), $\varepsilon_0 = 8.85 \times 10^{-12}$ F/m the permittivity of free space [58], e the charge of an electron, and A is the surface area of the electrode. The permittivity ε (~76) is determined from the dielectric measurement on sintered pellet, while the hole density $N_D = 3.53 \times 10^{20}$ cm^{-3} is determined from the slope.

The curve $C^{-2}(E)$ exhibits good linearity and it is represented in Figure 7. The potential $E_{fb} = (0.54\ V)$ is easily obtained by extrapolating the plot to infinite capacity ($C^{-2} = 0$). The positive slope confirms the n-type conduction.

The space charge width (W~3.45 nm) was calculated under optimal band bending at the interface ($E - E_{fb}$) using the following equation [59,60]:

$$W = \left(\frac{2\varepsilon\varepsilon_0(E - E_{fb})}{eN_D}\right)^{0.5} \quad (13)$$

The space charge width W is less than the diameter size D calculated from DRX, so the recombination of the pairs (e^-/h^+) is kept at a low level. The width of depletion extends over several crystallographic units, which is advantageous in photocatalysis.

Usually, the conduction band position of n-type semiconductors is 0.1 V above the flat band levels [37]. So, the conduction band ($E_{CB} = -5.19$ eV/0.44 V) indicates that the CB is composed mainly of oxides derived from Orbital 3D. Hence, the energy of the valance band ($E_{VB} = E_{CB} - E_g = -7.99$ eV/3.24 V).

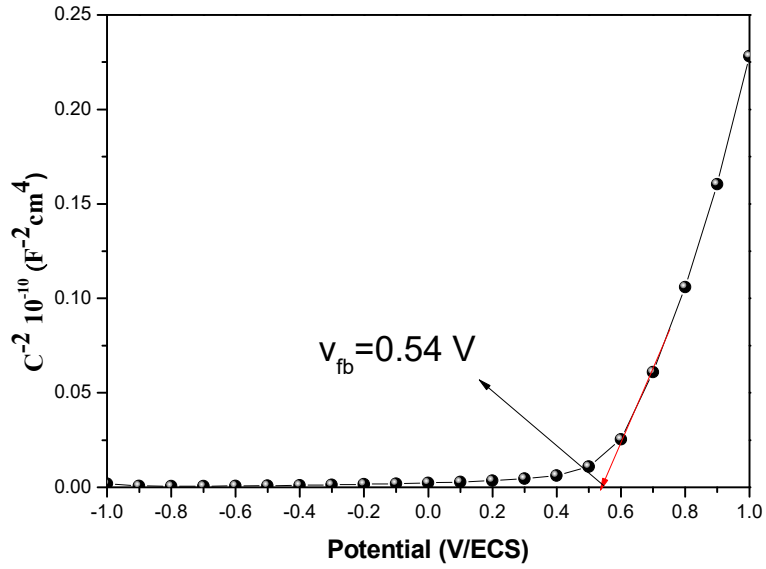

Figure 7. The capacitance-potential characteristic of $ZnBi_2O_4$ in NaOH (0.1 M) solution.

The diagram of electrochemical impedance spectroscopy (EIS) of the junction $ZnBi_2O_4$/NaOH electrolyte is modeled to an equivalent electrical circuit using the software Zview (Figure 8 Inset), corresponding to the contribution of the bulk, grains boundary, and ions diffusion. The Nyquist diagram is the plot of the imaginary part (Z_{im}) versus the real part (Z_{re}) related to the presence of a constant phase element (CPE) [61]:

$$Z = Q(jW)^{-n};\ n = \frac{1-2q}{p} \tag{14}$$

where Q is a frequency-independent constant, n is the homogeneity factor ($0 < n \leq 1$) related to the phase angle $\varphi = (n\pi/2)$. (Figure 8) illustrated the Nyquist diagram with the modeling results of the equivalent electrical circuit, which represent a semicircle associated with the charge transfer resistance (Rs = 1 kΩ cm^2) in series with a Constant Phase Element CPE ($CPE_T = 3.79 \times 10^{-3}$, $CPE_P = 0.3198$) and Warburg Element W_O ($W_{O_R} = 36315$, $W_{O_T} = 4.469$, $W_{O_P} = 0.78123$), in parallel with Rp the electrolyte solution (49 kΩ cm^2). The chi-squared and weighted sum of squares are 0.00186, 0.0392 respectively. The process is also represented in the Bode plan (log Z vs. log frequency) (Figure S9 in the Supplementary Data). The decrease in Z increasing the frequency indicates an enhanced electrical conductivity and a lowering of the potential barrier [57].

3.2. Photocatalytic Activity of the Catalyst

To research the photocatalyst efficiency under each source of light, the process of photolysis must be considered. In order to remove the impact of photolysis, a set of experiments were carried out without the catalyst ZBO in a 100 mL solution of CFX with a concentration of 10 mg/L at pH = 6 in each light irradiation UV, LED and solar light. Only a small percentage of CFX degradation, not exceedingly even 5% has been recorded by photolysis in all sources of light. So, it can be concluded that the photolysis impact could be ignored.

After neglecting the effect of photolysis, we performed the same set of experiments in the same conditions but in the presence of ZBO photocatalyst. Before exposing those experiments to the sources of irradiation, all sets have been mixed in the dark for 120 min to established the adsorption-desorption equilibrium. Figure 9 demonstrated the difference in degradation under different light sources. As can be shown, while the catalyst radiated by solar light, the CFX degradation rate reached 89% in just 30 min, while that for other sources was lower. ZBO has more efficient degradation in the solar light because the solar light contained all visible, UV and other light irradiation. It has the largest light

spectrum. Moreover, the intensity plays a role in this part as the solar light has great intensity (98 mW/cm^{-2}). The UV irradiated gives a good degradation performance within the time, giving an 88.1% degradation in 2 h. This difference can be due to the color and the gap energy of the catalyst (2.8 eV), which gives a higher light absorption in the range of 200–600 nm, which is very close to the UV region. For the sunlight, it has the greatest light spectrum also containing the UV region causing a rapid degradation for CFX. On the other hand, the LED containing only visible light for that only small degradation was observed with it. This result was confirmed the finding of the optical and dielectric characterization as demonstrated previously in the optical study. ZBO has shown more efficiency in the degradation compared to our previous research about the degradation of CFX using ZnO [62] which gives a 60% degradation rate in 3 h. That can be explained by the ZBO bandgap (2.8 eV) being smaller than ZnO. Increasing the photocatalytic efficiency of semiconductors by lowering the bandgap and facilitating the separation of photo-generated electrons and holes is a difficult task.

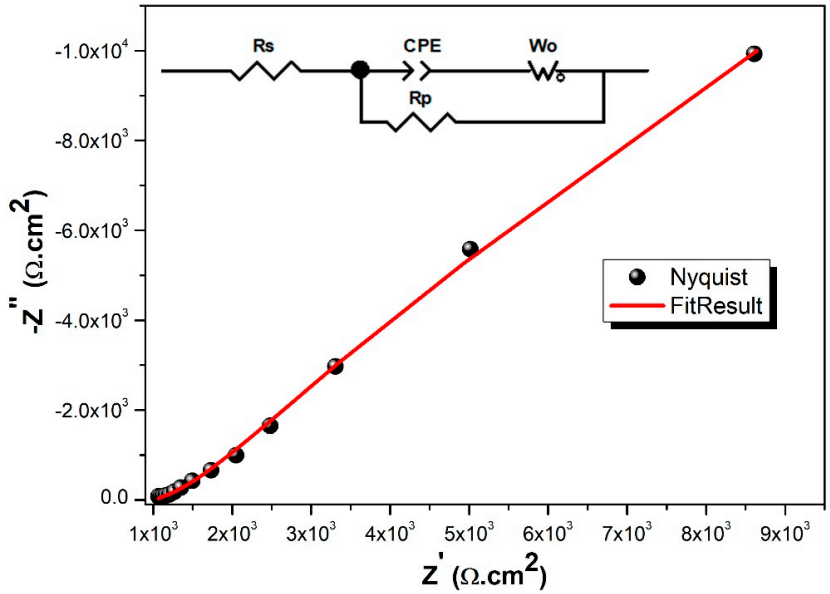

Figure 8. The EIS (Nyquist) diagram of $ZnBi_2O_4$ in NaOH solution, inset: equivalent electrical circuit.

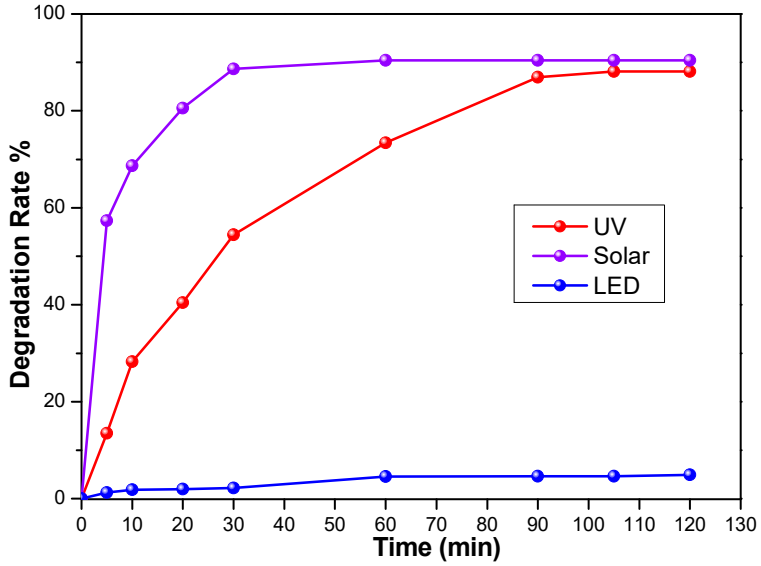

Figure 9. The photocatalytic activity of $ZnBi_2O_4$ under UV, sunlight and LED lamp: CCFX = 10 ppm, pH ~6, T = 25 °C and catalyst dose = 1 g/L.

3.3. Energy Diagram and Suggested Mechanism

In general, a photocatalyst may assign photodegradation of organic substances to different reaction pathways regulated by different active species such as $OH^{\bullet}$, $O_2^{\bullet}$, and holes (h^+) [62]. As demonstrated in the literature, ZBO can be quickly excited and the e^-/h^+ pairs produced because of its narrow bandgap [37]. This catalyst is a successful choice for the photodegradation of antibiotics as an electron reservoir [28]. In previous works [13,63–65], both holes and hydroxyl radicals have been suggested to be active oxidizing agents responsible for removing organic substances. The photodegradation mechanism was illustrated in both Figure 10 and Equations (15) to (18):

$$ZnBi_2O_4 + h\upsilon \rightarrow ZnBi_2O_4{}^* + e^- + h^+ \quad (15)$$

$$H_2O + h^+ \rightarrow OH^* + H^+ \quad (16)$$

$$O_2 + e^- \rightarrow O_2{}^{-*} \quad (17)$$

$$CFX + OH^* \text{ and } O_2{}^{-*} \rightarrow CO_2 + H_2O + \text{other small intermediate by products} \quad (18)$$

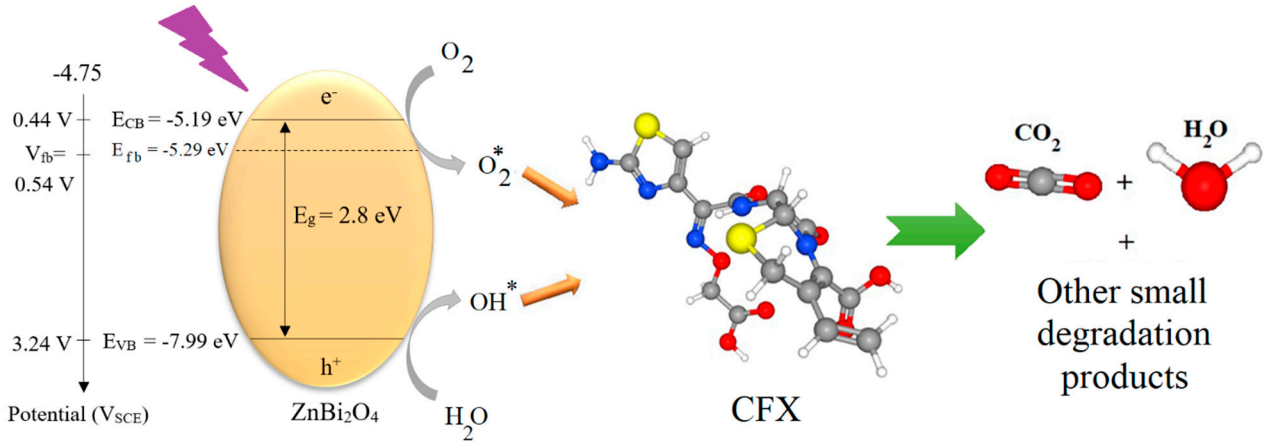

Figure 10. Energy diagram and suggested mechanism for CFX degradation by ZBO nanoparticles.

4. Conclusions

In this research, nanoparticles of $ZnBi_2O_4$ have successfully been synthesized by co-precipitation and then described by different methods to distinguish the optical, dielectric, and electrochemical properties. Firstly, DRX and FTIR were used to confirm the obtaining of the spinal phase. Then, an SEM analysis was performed to investigate the morphology of the nanoparticles ZBO; uniform shapes have been observed. An optical study was done to investigate ZBO optical and dielectric proprieties, which shows that this catalyst has good photocatalytic activity in the UV region with a gap band (~2.8 eV). Additionally, electrochemical characterizations were investigated in order to determine the type of catalyst, define the energetic diagram, and determine the location of the conduction and valence bands. An *n*-type semiconductor with a flat band potential of 0.54 V_{SCE} was discovered. The activity of this prepared photocatalyst was then checked for photodegradation of the Cefixime antibiotic under various light sources to demonstrate the finding of the optical characterization. The results revealed that the ZBO catalyst could lead to 89% of CFX degradation under solar light in only 30 min and 88% under UV irradiation after 2 h. Those results indicate that the catalyst can be a modern catalyst candidate for the removal of organic contaminants in water under solar radiation. We conclude with an outlook on future research, since this catalyst has demonstrated strong photocatalytic properties. It will be tested for the inactivation of bacteria and other microorganisms.

Supplementary Materials: The following are available online at https://www.mdpi.com/article/10.3390/app11093975/s1, Figure. S1 Chemical formula of the antibiotic Cefixime, Figure. S2 UV–visible spectra of Cefixime (10 mg/L), Figure. S3 UV-visible spectrum of $ZnBi_2O_4$, Figure. S4 Spectral distribution of n (λ) and K (λ), Figure. S5 Variation of SELF and VELF as a function of the energy (hν), Figure. S6 ε_r as function of λˆ2, Figure. S7 Variation of the real and imaginary parts of the optical conductivity as a function of the energy (hν), Figure. S8 Semi-logarithmic plot over $ZnBi_2O_4$ electrode, Figure. S9 Bode plan (log Z vs. log frequency).

Author Contributions: Conceptualization, O.B. and H.K.; methodology, A.A.; software, O.B.; validation, A.A.A. (Aymen Amine Assadi) and A.A.; formal analysis, M.T.; investigation, O.B.; resources, N.N.; data curation, O.B.; writing—original draft preparation, O.B., A.A.A. (Aymen Amine Assadi) and A.A.; writing—review and editing, O.B., A.A.A. (Aymen Amine Assadi) and A.A.; visualization, A.A.A. (Achraf Amir Assadi) and M.A.; supervision, A.A.A. (Aymen Amine Assadi) and A.A.; All authors have read and agreed to the published version of the manuscript.

Funding: This research received no external funding.

Institutional Review Board Statement: Not applicable.

Informed Consent Statement: Not applicable.

Data Availability Statement: Not applicable.

Acknowledgments: This work was financially supported by both the Faculties of Mechanical Engineering and Process Engineering and Chemistry.

Conflicts of Interest: The authors declare that they have no conflict of interest.

References

1. Kaczala, F.E.; Blum, S. The Occurrence of Veterinary Pharmaceuticals in the Environment: A Review. *Curr. Anal. Chem.* **2015**, *12*, 169–182. [CrossRef]
2. Baaloudj, O.; Nasrallah, N.; Kebir, M.; Khezami, L.; Amrane, A.; Assadi, A.A. A comparative study of ceramic nanoparticles synthesized for antibiotic removal: Catalysis characterization and photocatalytic performance modeling. *Environ. Sci. Pollut. Res.* **2020**. [CrossRef]
3. Mostafaloo, R.; Mahmoudian, M.H.; Asadi-ghalhari, M. $BiFeO_3$/Magnetic nanocomposites for the photocatalytic degradation of ce fi xime from aqueous solutions under visible light. *J. Photochem. Photobiol. A Chem.* **2019**, *382*, 111926. [CrossRef]
4. Kümmerer, K. Antibiotics in the aquatic environment—A review—Part II. *Chemosphere* **2009**, *75*, 435–441. [CrossRef]
5. Elder, F.C.T.; Feil, E.J.; Snape, J.N.; Gaze, W.H.; Kasprzyk-Hordern, B.A. The role of stereochemistry of antibiotic agents in the development of antibiotic resistance in the environment. *Environ. Int.* **2020**, *139*, 105681. [CrossRef]
6. Liu, M.; Ni, H.; Yang, L.; Chen, G.; Yan, X.; Leng, X.; Liu, P.; Li, X. Pretreatment of swine manure containing β-lactam antibiotics with whole-cell biocatalyst to improve biogas production. *J. Clean. Prod.* **2019**, *240*, 118070. [CrossRef]
7. Littmann, J.; Buyx, A.; Cars, O. Antibiotic resistance: An ethical challenge. *Int. J. Antimicrob. Agents* **2015**, *46*, 359–361. [CrossRef] [PubMed]
8. Li, B.; Zhang, T. Biodegradation and adsorption of antibiotics in the activated sludge process. *Environ. Sci. Technol.* **2010**, *44*, 3468–3473. [CrossRef] [PubMed]
9. Gao, Y.; Li, Y.; Zhang, L.; Huang, H.; Hu, J.; Shah, S.M.; Su, X. Adsorption and removal of tetracycline antibiotics from aqueous solution by graphene oxide. *J. Colloid Interface Sci.* **2012**, *368*, 540–546. [CrossRef] [PubMed]
10. Chen, W.R.; Huang, C.H. Adsorption and transformation of tetracycline antibiotics with aluminum oxide. *Chemosphere* **2010**, *79*, 779–785. [CrossRef] [PubMed]
11. Kamagate, M.; Amin Assadi, A.; Kone, T.; Coulibaly, L.; Hanna, K. Activation of persulfate by irradiated laterite for removal of fluoroquinolones in multi-component systems. *J. Hazard. Mater.* **2018**, *346*, 159–166. [CrossRef] [PubMed]
12. Lou, W.; Kane, A.; Wolbert, D.; Rtimi, S.; Assadi, A.A. Study of a photocatalytic process for removal of antibiotics from wastewater in a falling film photoreactor: Scavenger study and process intensification feasibility. *Chem. Eng. Process. Process Intensif.* **2017**, *122*, 213–221. [CrossRef]
13. Aboudalle, A.; Fourcade, F.; Assadi, A.A.; Domergue, L.; Djelal, H.; Lendormi, T.; Taha, S.; Amrane, A. Reactive oxygen and iron species monitoring to investigate the electro-Fenton performances. Impact of the electrochemical process on the biodegradability of metronidazole and its by-products. *Chemosphere* **2018**, *199*, 486–494. [CrossRef] [PubMed]
14. Reyes, C.; Fernández, J.; Freer, J.; Mondaca, M.A.; Zaror, C.; Malato, S.; Mansilla, H.D. Degradation and inactivation of tetracycline by TiO_2 photocatalysis. *J. Photochem. Photobiol. A Chem.* **2006**, *184*, 141–146. [CrossRef]
15. Zuo, S.; Chen, Y.; Liu, W.; Yao, C.; Li, X.; Li, Z.; Ni, C.; Liu, X. A facile and novel construction of attapulgite/Cu_2O/Cu/g-C_3N_4 with enhanced photocatalytic activity for antibiotic degradation. *Ceram. Int.* **2017**, *43*, 3324–3329. [CrossRef]

16. Wang, W.; Fang, J.; Chen, H.; Bao, N.; Lu, C. Rice-husk-derived mesoporous 0D/2D C_3N_4 isotype heterojunction with improved quantum effect for photodegradation of tetracycline antibiotics. *Ceram. Int.* **2019**, *45*, 2234–2240. [CrossRef]
17. Martins, A.C.; Cazetta, A.L.; Pezoti, O.; Souza, J.R.B.; Zhang, T.; Pilau, E.J.; Asefa, T.; Almeida, V.C. Sol-gel synthesis of new TiO_2/activated carbon photocatalyst and its application for degradation of tetracycline. *Ceram. Int.* **2017**, *43*, 4411–4418. [CrossRef]
18. Ma, Z.; Hu, L.; Li, X.; Deng, L.; Fan, G.; He, Y. A novel nano-sized MoS_2 decorated Bi_2O_3 heterojunction with enhanced photocatalytic performance for methylene blue and tetracycline degradation. *Ceram. Int.* **2019**, *45*, 15824–15833. [CrossRef]
19. Hong, Y.; Ren, A.; Jiang, Y.; He, J.; Xiao, L.; Shi, W. Sol-gel synthesis of visible-light-driven $Ni_{(1-x)}Cu_{(x)}Fe_2O_4$ photocatalysts for degradation of tetracycline. *Ceram. Int.* **2015**, *41*, 1477–1486. [CrossRef]
20. Ene, C.D.; Patrinoiu, G.; Munteanu, C.; Ene, R.; Chifiriuc, M.C.; Carp, O. Multifunctional ZnO materials prepared by a versatile green carbohydrate-assisted combustion method for environmental remediation applications. *Ceram. Int.* **2019**, *45*, 2295–2302. [CrossRef]
21. Yu, B.; Meng, F.; Khan, M.W.; Qin, R.; Liu, X. Synthesis of hollow TiO_2@g-C_3N_4/Co_3O_4 core-shell microspheres for effective photooxidation degradation of tetracycline and MO. *Ceram. Int.* **2020**. [CrossRef]
22. Homem, V.; Santos, L. Degradation and removal methods of antibiotics from aqueous matrices—A review. *J. Environ. Manag.* **2011**, *92*, 2304–2347. [CrossRef] [PubMed]
23. Eddya, M.; Tbib, B.; El-Hami, K. Synthesis and X-ray diffraction studies of new photocatalyst $Zn_{1-x}Pb_xBi_2O_4$. *J. Mater. Environ. Sci.* **2018**, *15*, 1661–1664. [CrossRef]
24. Pant, B.; Pant, H.R.; Barakat, N.A.M.; Park, M.; Jeon, K.; Choi, Y.; Kim, H.Y. Carbon nanofibers decorated with binary semiconductor (TiO_2/ZnO) nanocomposites for the effective removal of organic pollutants and the enhancement of antibacterial activities. *Ceram. Int.* **2013**, *39*, 7029–7035. [CrossRef]
25. Pant, B.; Ojha, G.P.; Kim, H.Y.; Park, M.; Park, S.J. Fly-ash-incorporated electrospun zinc oxide nanofibers: Potential material for environmental remediation. *Environ. Pollut.* **2019**, *245*, 163–172. [CrossRef]
26. Tho, N.T.M.; Khanh, D.N.N.; Thang, N.Q.; Lee, Y.I.; Phuong, N.T.K. Novel reduced graphene oxide/$ZnBi_2O_4$ hybrid photocatalyst for visible light degradation of 2,4-dichlorophenoxyacetic acid. *Environ. Sci. Pollut. Res.* **2020**, *27*, 11127–11137. [CrossRef] [PubMed]
27. Chen, P.; Liu, H.; Cui, W.; Lee, S.C.; Wang, L.; Dong, F. Bi-based photocatalysts for light-driven environmental and energy applications: Structural tuning, reaction mechanisms, and challenges. *EcoMat* **2020**, *2*, 1–31. [CrossRef]
28. Thi Mai Tho, N.; The Huy, B.; Nha Khanh, D.N.; Quoc Thang, N.; Thi Phuong Dieu, N.; Dai Duong, B.; Thi Kim Phuong, N. Mechanism of Visible-Light Photocatalytic Mineralization of Indigo Carmine Using $ZnBi_2O_4$-Bi_2S_3 Composites. *ChemistrySelect* **2018**, *3*, 9986–9994. [CrossRef]
29. Nithya, R.; Ayyappan, S. Novel exfoliated graphitic-C_3N_4 hybridised $ZnBi_2O_4$ (g-C_3N_4/$ZnBi_2O_4$) nanorods for catalytic reduction of 4-Nitrophenol and its antibacterial activity. *J. Photochem. Photobiol. A Chem.* **2020**, *398*. [CrossRef]
30. Kumar, K.V.; Shilpa, C.H.; Rama, C.K.; Rajesham, K.A. Synthesis & Structural Characteristics of $ZnBi_2O_4$ Nanoparticles Prepared by Citrate-Gel Auto Combustion Method. *Int. J. Nanoparticle Res.* **2018**, 1–7. [CrossRef]
31. Zhang, J.; Jiang, Y.; Gao, W.; Hao, H. Synthesis and visible photocatalytic activity of new photocatalyst MBi_2O_4 (M = Cu, Zn). *J. Mater. Sci. Mater. Electron.* **2015**, *26*, 1866–1873. [CrossRef]
32. Tho, N.T.M.; Huy, B.T.; Khanh, D.N.N.; Ha, H.N.N.; Huy, V.Q.; Vy, N.T.T.; Huy, D.M.; Dat, D.P.; Phuong, N.T.K. Facile synthesis of $ZnBi_2O_4$-graphite composites as highly active visible-light photocatalyst for the mineralization of rhodamine B. *Korean J. Chem. Eng.* **2018**, *35*, 2442–2451. [CrossRef]
33. Yang, Q.; Zhong, J.; Li, J.; Chen, J.; Xiang, Z.; Wang, T.; Li, M. Photo-induced charge separation properties of NiO/Bi_2O_3 heterojuctions with efficient simulated solar-driven photocatalytic performance. *Curr. Appl. Phys.* **2017**, *17*, 484–487. [CrossRef]
34. He, R.; Xu, D.; Cheng, B.; Yu, J.; Ho, W. Review on nanoscale Bi-based photocatalysts. *Nanoscale Horizons* **2018**, *3*, 464–504. [CrossRef] [PubMed]
35. Mohamed, R.M.; Barakat, M.A. Enhancement of photocatalytic activity of ZnO/SiO_2 by nanosized Pt for photocatalytic degradation of phenol in wastewater. *Int. J. Photoenergy* **2012**, *2012*. [CrossRef]
36. Martinez Suarez, C.; Hernández, S.; Russo, N. $BiVO_4$ as photocatalyst for solar fuels production through water splitting: A short review. *Appl. Catal. A Gen.* **2015**, *504*, 158–170. [CrossRef]
37. Habibi-yangjeh, A.; Pirhashemi, M.; Ghosh, S. ZnO/$ZnBi_2O_4$ nanocomposites with p-n heterojunction as durable visible-light-activated photocatalysts for efficient removal of organic pollutants. *J. Alloys Compd.* **2020**, 154229. [CrossRef]
38. Sheydaei, M.; Shiadeh, H.R.K.; Ayoubi-Feiz, B.; Ezzati, R. Preparation of nano N-TiO_2/graphene oxide/titan grid sheets for visible light assisted photocatalytic ozonation of cefixime. *Chem. Eng. J.* **2018**, *353*, 138–146. [CrossRef]
39. Shooshtari, N.M.; Ghazi, M.M. An investigation of the photocatalytic activity of nano A-Fe_2O_3/ZnO on the photodegradation of cefixime trihydrate. *Chem. Eng. J.* **2017**, *315*, 527–536. [CrossRef]
40. Mastanamma, S.K.; Reehana, S.K.; Prudhvi, L.; Kiran, R. UV spectrophotometric method for the determination of sirolimus in bulk and its dosage form. *Res. J. Pharm. Technol.* **2019**, *12*, 1655–1658. [CrossRef]
41. Sabri, K.; Rais, A.; Taibi, K.; Moreau, M.; Ouddane, B.; Addou, A. Structural Rietveld refinement and vibrational study of $MgCr_xFe_{2-x}O_4$ spinel ferrites. *Phys. B Condens. Matter* **2016**, *501*, 38–44. [CrossRef]
42. Geng, Q.; Zhao, X.; Gao, X.; Yang, S.; Liu, G. Low-temperature combustion synthesis of $CuCr_2O_4$ spinel powder for spectrally selective paints. *J. Sol-Gel Sci. Technol.* **2012**, *61*, 281–288. [CrossRef]

43. Ramezanalizadeh, H.; Peymanfar, R.; Khodamoradipoor, N. Design and development of a novel lanthanum inserted $CuCr_2O_4$ nanoparticles photocatalyst for the efficient removal of water pollutions. *Optik* **2019**, *180*, 113–124. [CrossRef]
44. Mobini, S.; Meshkani, F.; Rezaei, M. Surfactant-assisted hydrothermal synthesis of $CuCr_2O_4$ spinel catalyst and its application in CO oxidation process. *J. Environ. Chem. Eng.* **2017**, *5*, 4906–4916. [CrossRef]
45. Viruthagiri, G.; Kannan, P. Visible light mediated photocatalytic activity of cobalt doped Bi_2O_3 nanoparticles. *J. Mater. Res. Technol.* **2019**, *8*, 127–133. [CrossRef]
46. Yang, J.; Xie, T.; Liu, C.; Xu, L. Facile fabrication of dumbbell-like β-Bi_2O_3/ graphene nanocomposites and their highly efficient photocatalytic activity. *Materials* **2018**, *11*, 1359. [CrossRef] [PubMed]
47. Benrighi, Y.; Nasrallah, N.; Chaabane, T.; Sivasankar, V.; Darchen, A.; Baaloudj, O. Photocatalytic performances of $ZnCr_2O_4$ nanoparticles for cephalosporins removal: Structural, optical and electrochemical properties. *Opt. Mater.* **2021**, *115*. [CrossRef]
48. Belabed, C.; Bellal, B.; Tab, A.; Dib, K.; Trari, M. Optik Optical and dielectric properties for the determination of gap states of the polymer semiconductor: Application to photodegradation of organic pollutants. *Opt. Int. J. Light Electron Opt.* **2018**, *160*, 218–226. [CrossRef]
49. Gherbi, R.; Bessekhouad, Y.; Trari, M. Structure, optical and transport properties of Mg-doped $ZnMn_2O_4$. *J. Alloys Compd.* **2016**, *655*, 188–197. [CrossRef]
50. Serbetçi, Z.; El-Nasser, H.M.; Yakuphanoglu, F. Photoluminescence and refractive index dispersion properties of ZnO nanofibers grown by sol-gel method. *Spectrochim. Acta Part A Mol. Biomol. Spectrosc.* **2012**, *86*, 405–409. [CrossRef]
51. Sakr, G.B.; Yahia, I.S.; Fadel, M.; Fouad, S.S. Optical spectroscopy, optical conductivity, dielectric properties and new methods for determining the gap states of CuSe thin films. *J. Alloy. Compd.* **2010**, *507*, 557–562. [CrossRef]
52. El-nahass, M.M.; Sallam, M.M.; Rahman, S.A.; Ibrahim, E.M. Optical, electrical conduction and dielectric properties of $TlGaSe_2$ layered single crystal. *Solid State Sci.* **2006**, *8*, 488–499. [CrossRef]
53. Fadel, M.; Labib, H.H.; Afifi, M.A. Optical properties of amorphous Ge Se Tl system films. *Thin Solid Film* **2001**, *386*, 99–104.
54. Johar, M.A.; Afzal, R.A.; Alazba, A.A.; Manzoor, U. Photocatalysis and Bandgap Engineering Using ZnO Nanocomposites. *Adv. Mater. Sci. Eng.* **2015**, *2015*. [CrossRef]
55. El-nahass, M.M.; Farag, A.A.M.; Ibrahim, E.M.; Abd-el-rahman, S. Structural, optical and electrical properties of thermally evaporated Ag_2S thin films. *Vacuum* **2004**, *72*, 453–460. [CrossRef]
56. Meziani, D.; Reziga, A.; Rekhila, G.; Bellal, B.; Trari, M. Hydrogen evolution under visible light over $LaCoO_3$ prepared by chemical route. *Energy Convers. Manag.* **2014**, *82*, 244–249. [CrossRef]
57. Benreguia, N.; Barnabé, A.; Trari, M. Sol–gel synthesis and characterization of the delafossite $CuAlO_2$. *J. Sol-Gel Sci. Technol.* **2015**, *75*, 670–679. [CrossRef]
58. Manohar, A.; Krishnamoorthi, C. Structural, optical, dielectric and magnetic properties of $CaFe_2O_4$ nanocrystals prepared by solvothermal reflux method. *J. Alloys Compd.* **2017**, *722*, 818–827. [CrossRef]
59. Lahmar, H.; Kebir, M.; Nasrallah, N.; Trari, M. Photocatalytic reduction of Cr(VI) on the new hetero-system $CuCr_2O_4$/ZnO. *J. Mol. Catal. A Chem.* **2012**, *353–354*, 74–79. [CrossRef]
60. Kenfoud, H.; Nasrallah, N.; Baaloudj, O.; Meziani, D.; Chaabane, T.; Trari, M. Photocatalytic reduction of Cr(VI) onto the spinel $CaFe_2O_4$ nanoparticles. *Optik* **2020**, *223*, 165610. [CrossRef]
61. Hammache, Z.; Soukeur, A.; Omeiri, S.; Bellal, B.; Trari, M. Physical and photo-electrochemical properties of $MgFe_2O_4$ prepared by sol gel route: Application to the photodegradation of methylene blue. *J. Mater. Sci. Mater. Electron.* **2019**, *30*, 5375–5382. [CrossRef]
62. Baaloudj, O.; Nasrallah, N.; Kebir, M.; Guedioura, B.; Amrane, A.; Nguyen-Tri, P.; Nanda, S.; Assadi, A.A. Artificial neural network modeling of cefixime photodegradation by synthesized $CoBi_2O_4$ nanoparticles. *Environ. Sci. Pollut. Res.* **2020**. [CrossRef]
63. Abou Dalle, A.; Domergue, L.; Fourcade, F.; Assadi, A.A.; Djelal, H.; Lendormi, T.; Soutrel, I.; Taha, S.; Amrane, A. Efficiency of DMSO as hydroxyl radical probe in an Electrochemical Advanced Oxidation Process − Reactive oxygen species monitoring and impact of the current density. *Electrochim. Acta* **2017**, *246*, 1–8. [CrossRef]
64. Belaissa, Y.; Nibou, D.; Assadi, A.A.; Bellal, B.; Trari, M. A new hetero-junction p-CuO/n-ZnO for the removal of amoxicillin by photocatalysis under solar irradiation. *J. Taiwan Inst. Chem. Eng.* **2016**, *68*, 254–265. [CrossRef]
65. Zadi, T.; Assadi, A.A.; Nasrallah, N.; Bouallouche, R.; Tri, P.N.; Bouzaza, A.; Azizi, M.M.; Maachi, R.; Wolbert, D. Treatment of hospital indoor air by a hybrid system of combined plasma with photocatalysis: Case of trichloromethane. *Chem. Eng. J.* **2018**, *349*, 276–286. [CrossRef]